Supporting Information

Boosting P-$CoMoO_3/MoO_2$ hydrogen evolution via water molecule dissociation by MoO_2 and H_2 desorption by $CoMoO_3$

Xue Yang [a, b], Liangkun Qiu [a, c], Yan Zhang [d], Ao Dong [a], Chenyang Guo [a], Shuo Zhang [a], Yunjin Song [a], Hongtao Gao [a, *], and Tianrong Zhan [a, *].

[a] Key Laboratory of Optic-electric Sensing and Analytical Chemistry for Life Science (Ministry of Education), College of Chemistry and Molecular Engineering, Qingdao University of Science and Technology, Qingdao 266042, China

[b] Hebei Minzu Normal University, Chengde 067000, China.

[c] Shandong Environmental Protection Development Group Science and Technology Innovation Co., Ltd.

[d] SINOPEC Qingdao Safety Engineering Institute, Qingdao 266042, China

* Corresponding author, Tel & Fax: +86-532-84022990

E-mail address: gaohtao@qust.edu.cn (H. Gao)

trzhan@qust.edu.cn (T. Zhan)

EXPERIMENTAL SECTION

Materials and reagents

The potassium hydroxide (KOH), sodium monophosphate ($NaH_2PO_2 \cdot H_2O$), ammonium molybdate ($(NH_4)_6Mo_7O_{24} \cdot 4H_2O$), and the ethanol were purchased from Sinopharm Chemical Reagent Co., Ltd. The hydrochloric acid (HCl) was obtained from Xilong Scientific Co., Ltd. The cobalt nitrate ($Co(NO_3)_2 \cdot 6H_2O$) was purchased from the company of Macklin Chemical Reagent. Ni foam (NF) was obtained from Shengernuo Technology Co., Ltd. Deionized (DI) water with resistivity > 18 MΩ cm^{-1} was used.

Synthesis of $CoMoO_4$/NF

Ni foam (NF) of 1.5 cm × 4 cm was first ultrasonically cleaned with 1M HCl, DI water, and ethanol for 20, 5, and 20 min, respectively. Then, 0.5 mmol $(NH_4)_6Mo_7O_{24} \cdot 4H_2O$ and 2 mmol $Co(NO_3)_2 \cdot 6H_2O$ were dissolved in 50 mL DI water with stirring. The solution and NF were transferred to a 100 mL Teflon autoclave and reacted at 150 ◦C for 6 h. After the autoclave was cooled to room temperature, the $CoMoO_4$/NF was taken out and washed 3 times with deionized water and ethanol, respectively. The obtained sample was kept in a vacuum oven.

Synthesis of P-$CoMoO_3$/MoO_2

A piece of $CoMoO_4$/NF and 6 mmol $NaH_2PO_2 \cdot H_2O$ were put into the tube furnace and $NaH_2PO_2 \cdot H_2O$ was placed upstream. After filling the quartz tube with Ar, the tube furnace heated to 500 ◦C at a heating rate of 5 ◦C/min and held for 1h. After the reaction, the furnace was naturally cooled to room temperature with Ar flow. The obtained P-$CoMoO_3$/MoO_2 was removed from the quartz tube and put into a vacuum-drying oven. For comparison, $CoMoO_4$-Ar was directly prepared from $CoMoO_4$/NF through calcination at 500 ◦C for 1 h without NaH_2PO_2.

Material characterizations

X-ray diffraction mapping characterized the samples' phase structure (XRD, Rigaku, Smartlab SE). Scanning electron microscopy (SEM, ZESSI, sigma 300) and transmission electron microscopy (TEM, JEOL, JEM-2100F) were used to characterize the morphology and elemental mapping images. The chemical composition was

determined by X-ray photoelectron spectroscopy (XPS, Thermo Fisher Scientific K-Alphah). Raman spectra were performed by a Raman system (Thermo Scientific DXR 2xi Micro-Raman). Elemental content was determined by inductively coupled plasma optical emission spectrometer (ICP-OES, Agilent 720ES).

Electrochemical measurement

All the electrochemical measurements were performed on a CHI 760D electrochemical workstation at 298K in 1 M KOH solution. The three-electrode cell was employed to measure electrochemical performance, with the sample (0.5 × 0.5 cm^2), an Hg/HgO electrode, and graphite utilized as the working electrode, the reference electrode, and the counter electrode, respectively. The measured potentials were calculated as reversible hydrogen electrode (RHE) corrected according to the equation:

$E_{RHE} = E_{Hg/HgO} + 0.098 + 0.059 \times pH$.

The linear sweep voltammetry (LSV) measurements were scanned at 2 mV s^{-1} with 95% iR-correction. The electrochemical impedance spectroscopy (EIS) was measured at -0.1 V (vs RHE). The double-layer capacitance (C_{dl}) was determined by cyclic voltammetry (CV) curves at scanning rates of 5 ~ 25 mV s^{-1} in 0.126 - 0.226 V (vs RHE). The chronoamperometric measurement was used to test the stability of the sample at -0.144 V (vs RHE).

The ECSA was calculated using the following:

$$ECSA = \frac{C_{dl}(Catalyst)}{C_s}$$

where C_s is the specific capacitance with the value of 0.04 mF cm^{-2} for an ideal flat surface [1].

To test the Faradaic efficiency (FE), the H_2 products were collected by drainage method. FE was obtained by comparing the measured value of H_2 produced by cathodic electrolysis with the calculated value of H_2, using the following equation:

$$FE(\%) = \frac{96485 \times 2 \times n(molH_2)}{Q} \times 100\%$$

where n (mol H_2) is the moles of H_2 calculated according to the volume of H_2 collected. Q was obtained from the electrochemical measurements. 96485 is Faraday constant.

Density functional theory calculations

All DFT calculations were implemented using the Vienna ab initio Simulation Package (VASP)[2-4]. The generalized gradient-corrected Perdew-Burke-Ernzerhof functional method (GGA-PBE) represents the electronic exchange and correlation. All computations used a plane-wave cutoff energy of 400 eV for the electronic wave function. The Brillouin zone was sampled by (4×3×1), (3×3×1), (3×3×1), (5×2×1), and (5×2×1) Monkhorst-Pack k-point mesh for geometries relaxed of MoO_2, $CoMoO_3$, $CoMoO_4$, $CoMoO_3$-MoO_2, and $CoMoO_4$-MoO_2 respectively[5], and K-point are doubled for electronic structure calculations. A vacuum layer of 20 Å was established in the z-axis direction to avoid the interaction between adjacent layers, and the force convergence criterion for structural optimization was set to 0.05 eV/Å. The spin polarization setting was turned on.

The free energy of the intermediates can be calculated using the computational hydrogen electrode method reported by Nørskov et al. According to the definition of the reversible hydrogen electrode, the free energy of H^+ (aq) + e^- in the standard state is equal to the free energy of 1/2 H_2 (g).

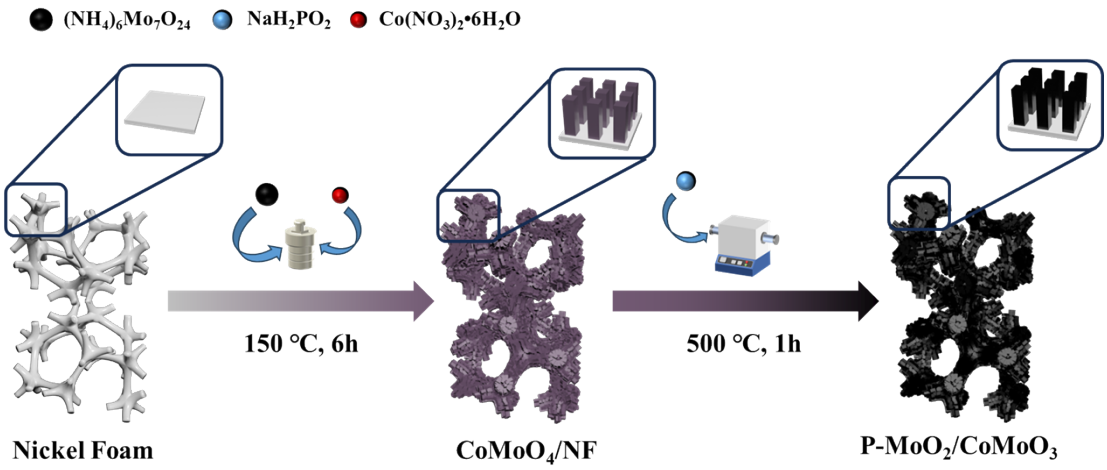

Figure S1. Schematic illustration of the fabrication process of P-$CoMoO_3$/MoO_2.

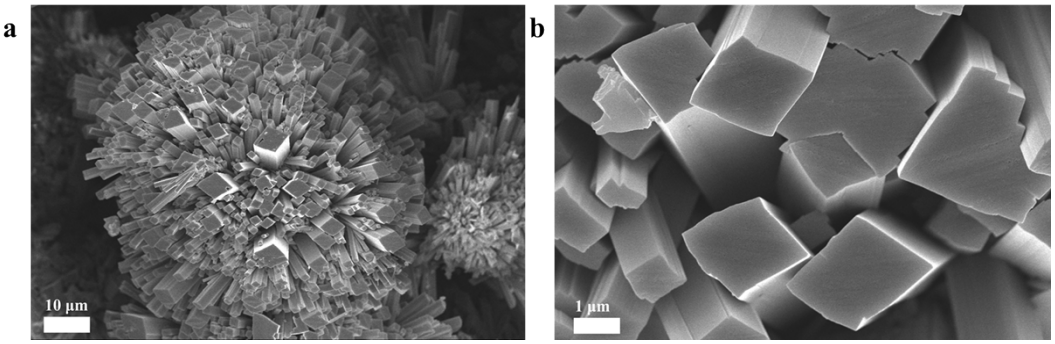

Figure S2. SEM images of $CoMoO_4$/NF at different magnifications

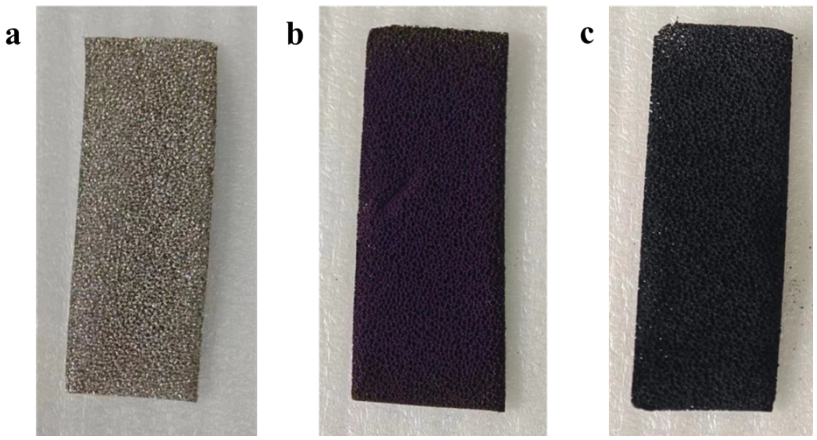

Figure S3. Photographs of the as-prepared catalyst (a) NF, (b) $CoMoO_4$, and (c) P-$CoMoO_3/MoO_2$.

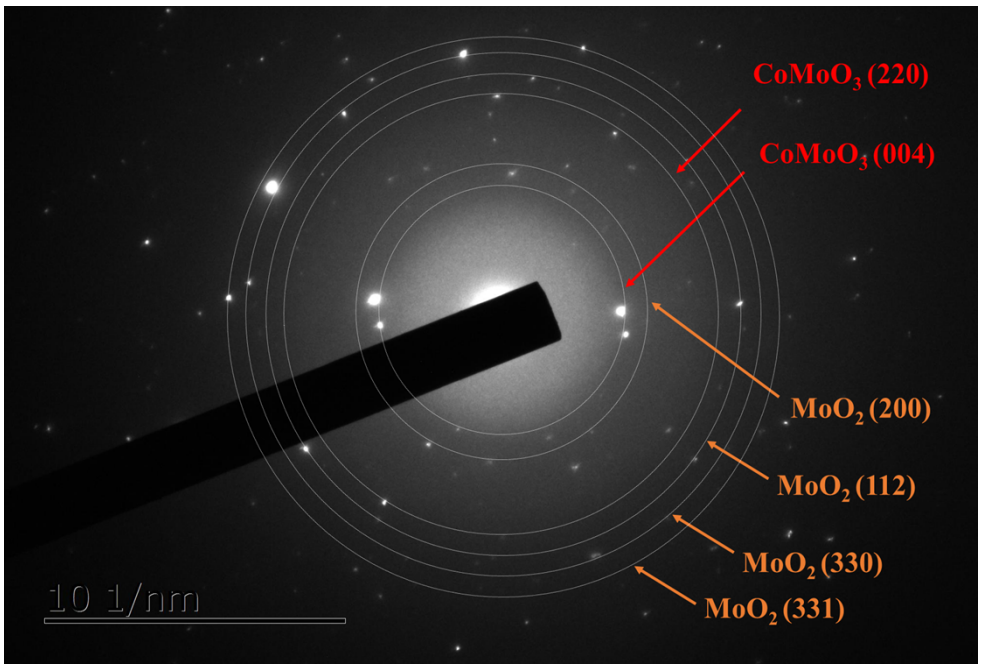

Figure S4. SAED images of P-$CoMoO_3$/MoO_2

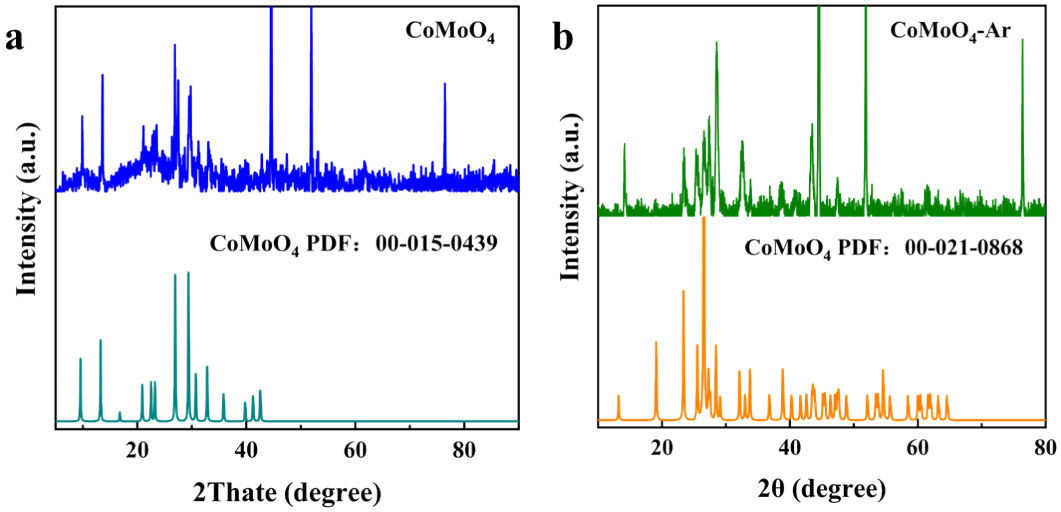

Figure S5. The XRD pattern of (a) $CoMoO_4$ and (b) $CoMoO_4$-Ar

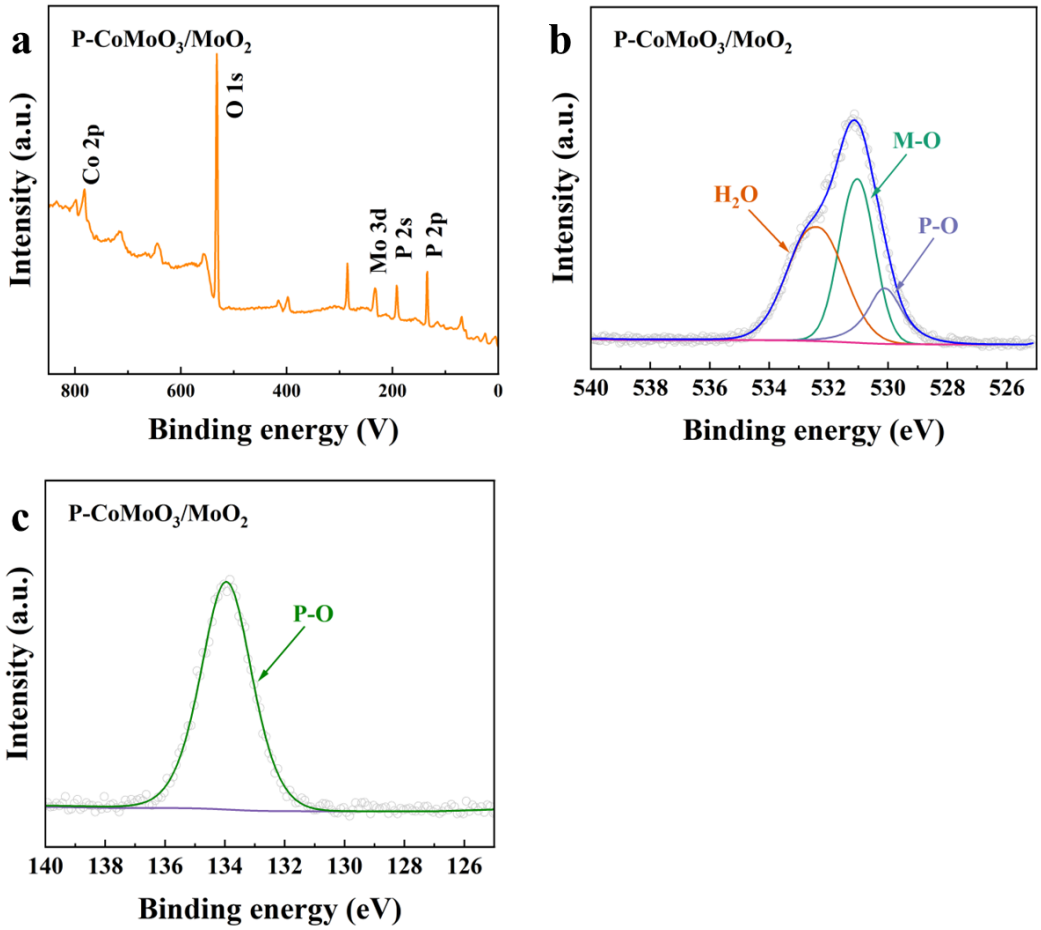

Figure S6. (a) XPS survey of as-prepared catalysts, the high-resolution XPS of (b) O 1s and (c) P 2p.

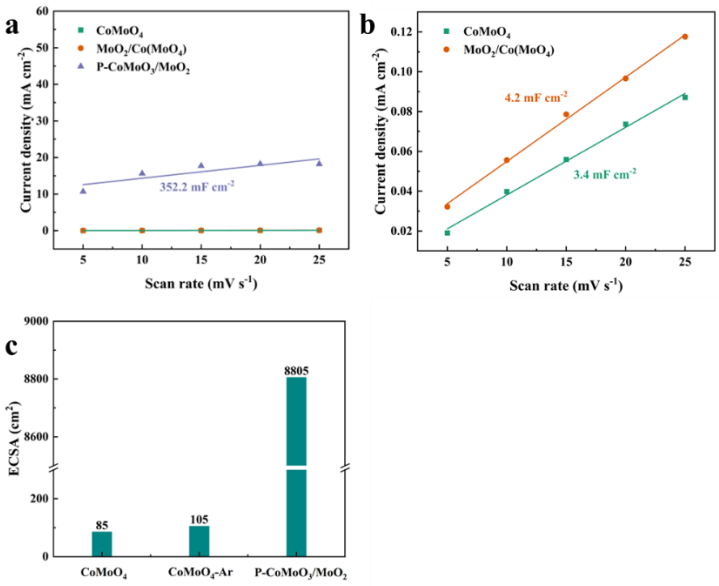

Figure S7. C_{dl} values of (a) $CoMoO_4$, $CoMoO_4$-Ar, and P-$CoMoO_3/MoO_2$, (b) $CoMoO_4$ and $CoMoO_4$-Ar, and ECSA of $CoMoO_4$, $CoMoO_4$-Ar, and P-$CoMoO_3/MoO_2$ (c).

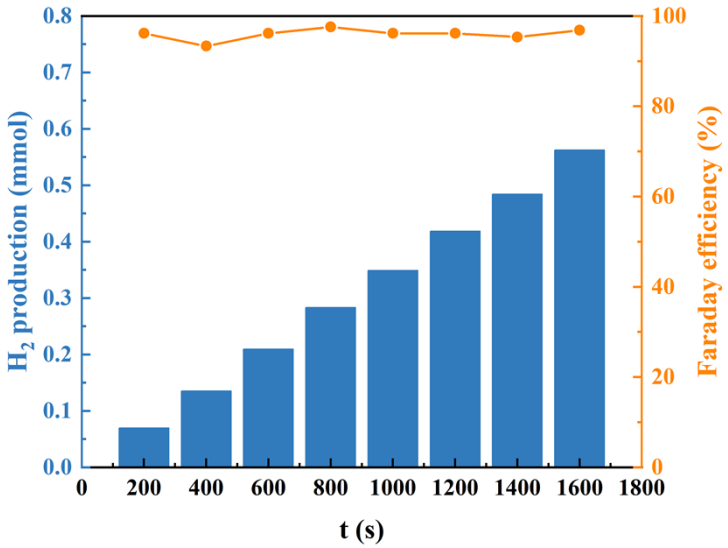

Figure S8. Hydrogen yield and Faraday efficiency of P-$CoMoO_3/MoO_2$.

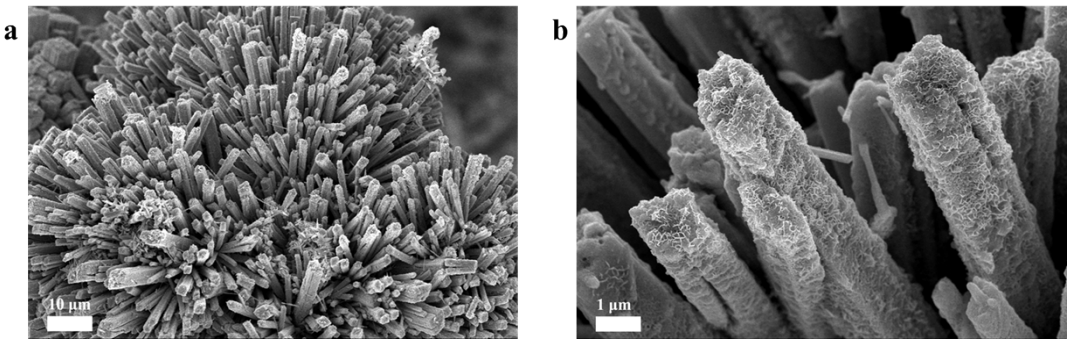

Figure S9. SEM images of P-$CoMoO_3$/MoO_2 after the stability test at different magnifications.

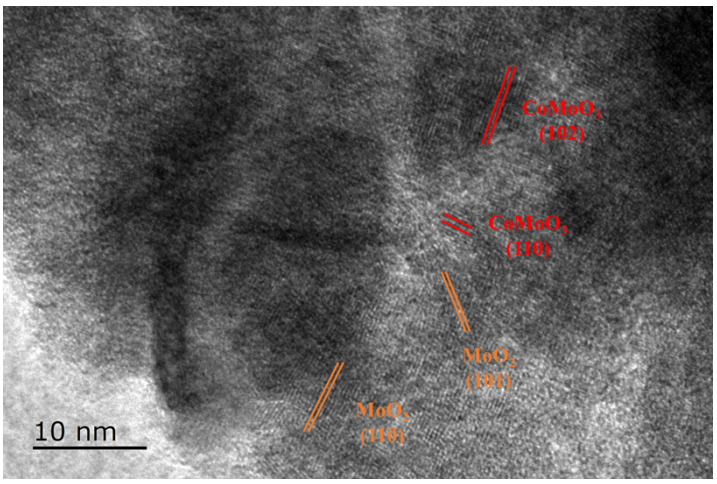

Figure S10. HRTEM images of P-$CoMoO_3$/MoO_2 after the stability test.

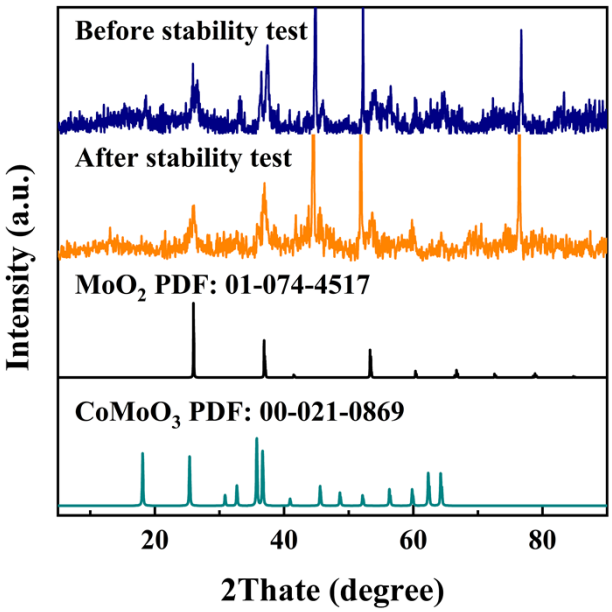

Figure S11. The XRD pattern of P-$CoMoO_3$/MoO_2 before and after the HER stability test.

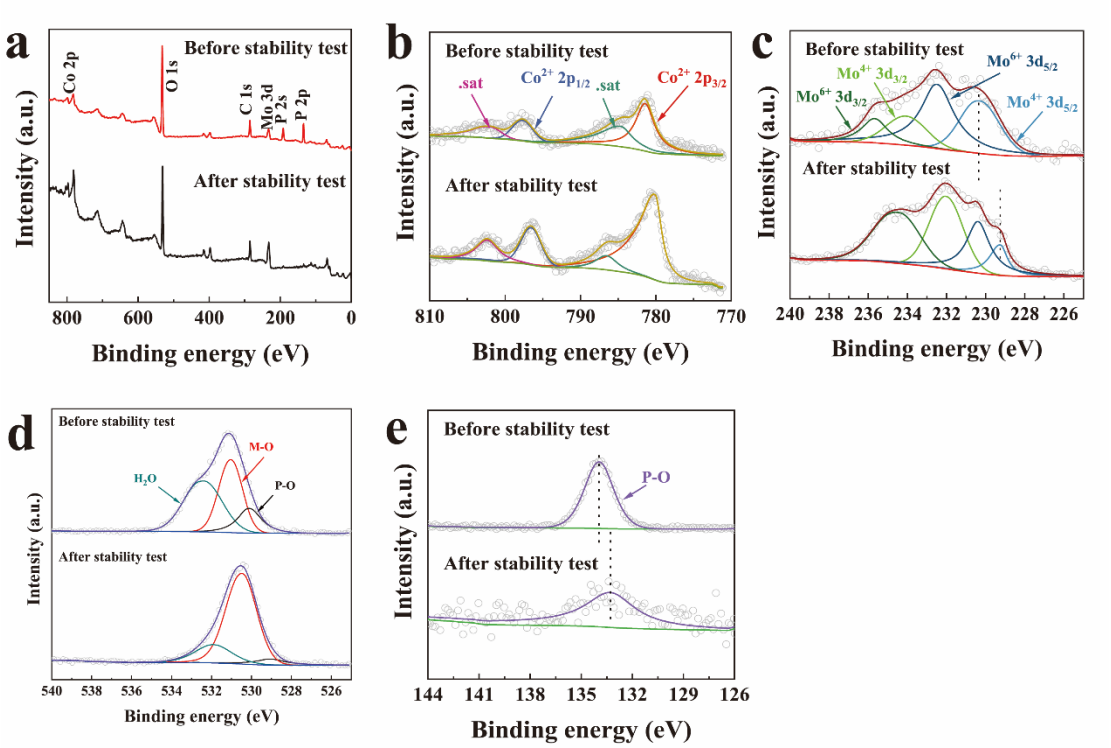

Figure S12. The XPS of (a) survey (b) Co 2p, (c) Mo 3d, (d) O 1s, and (e) P 2p of P-$CoMoO_3/MoO_2$ before and after the HER stability test.

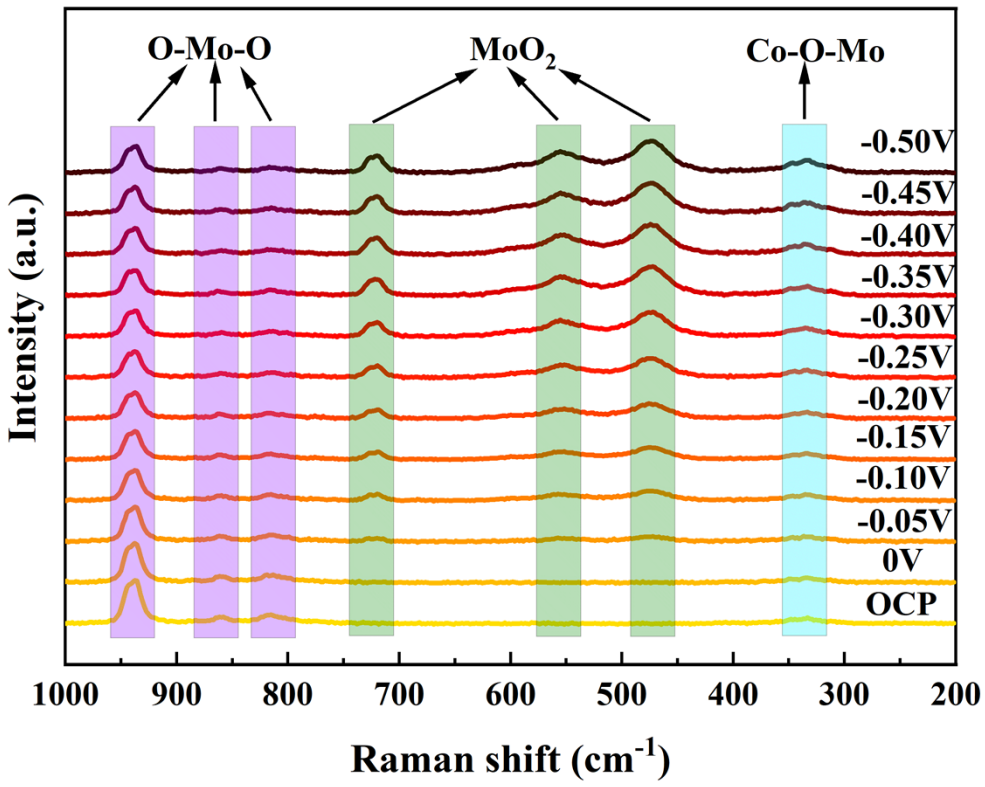

Figure S13. In-situ Raman spectra of P-$CoMoO_3/MoO_2$ were obtained at different potentials (vs RHE) in 1 M KOH.

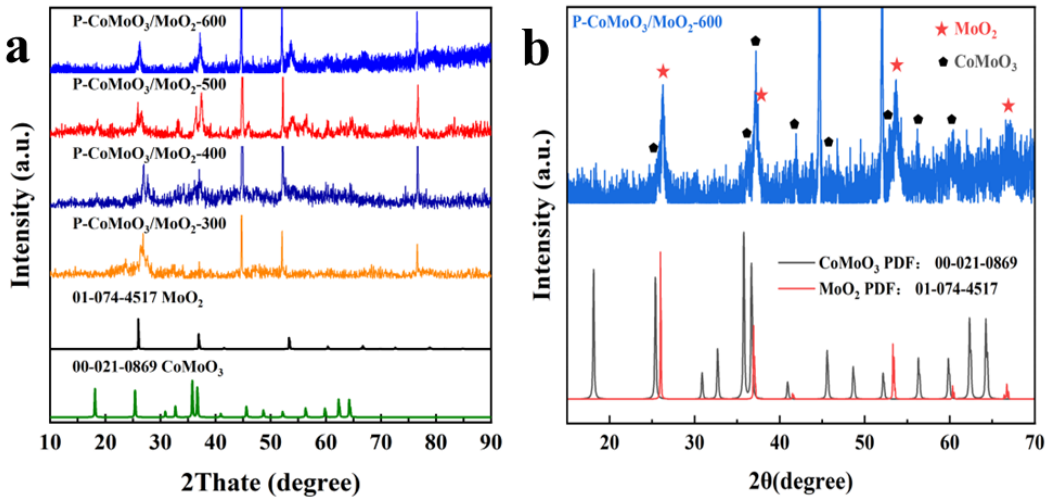

Figure S14. (a) XRD pattern of P-$CoMoO_3/MoO_2$-300, P-$CoMoO_3/MoO_2$-400, P-$CoMoO_3/MoO_2$-500, and P-$CoMoO_3/MoO_2$-600, (b) The XRD spectrum of P-$CoMoO_3/MoO_2$-600 at the range of 15-70 °.

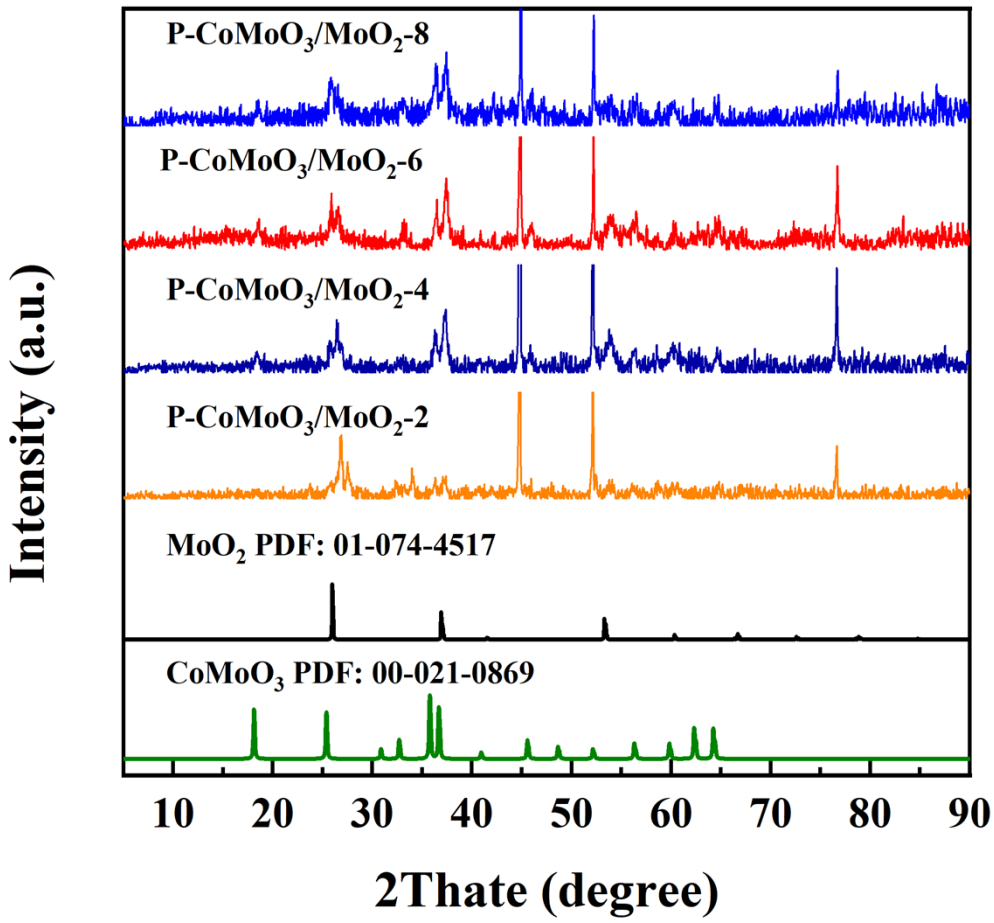

Figure S15. XRD pattern of P-$CoMoO_3/MoO_2$-2, P-$CoMoO_3/MoO_2$-4, P-$CoMoO_3/MoO_2$-6, and P-$CoMoO_3/MoO_2$-8.

Table S1. The radio of MoO_2 and $CoMoO_3$ in P-$CoMoO_3$/MoO_2 (n = 3)

	MoO_2/%	$CoMoO_3$/%
Before stability test	26.0 ± 0.1	74.0 ± 0.2

Table S2. HER activity comparison between the P-$CoMoO_3$/MoO_2 and other reported Mo-based electrocatalysts.

Catalyst	Electrolytes	Overpotential at 10 mA cm^{-2} (mV)	Overpotential at 100 mA cm^{-2} (mV)	Reference
$NiMo_{(pH10)}$	1M KOH	63.9	157.1	6
ECT-NiMo/$NiMoO_4$	1M KOH		196	7
NiMo-NW	1M KOH	30	125	8
$NiMoO_{4-x}$/MoO_2	1M KOH	41	106	9
$NiMoP_2$	1M KOH		195	10
NiMo HNRs/TiM	1M KOH	92	200	11
$Ni_{0.2}Mo_{0.8}N$/$NiMoP_2$/MoO_2@NC	1M KOH	48	173	12
$CoMo_2S_4$	1M KOH	55	150	13
CoMo/CoMoP/NF	1M KOH	29	104	14
Co_3Mo_2-LDH	1M KOH	165	325	15
Ru-CoMo/CFP	1M KOH	44	95	16
H-NMO/CMO/CF-450	1M KOH		87	17
Co_2P/$CoMoP_x$-NF	1M KOH	22	121	18
Fe-P-CMO	1M KOH		68	19
MoO_x/$Co(OH)_2$/NF	1M KOH	23	92	20
NiMo/$CoMoO_4$	1M KOH	102		21
CoP(MoP)-$CoMoO_3$@CN	1M KOH	198		22
a-$CoMoO_3$/Cu	1M KOH	31.6		23
Co–Mo/A-$Co(OH)_2$	1M KOH	47		24
N–CoMo-M	1M KOH	112		25
P-$CoMoO_3$/MoO_2	1M KOH	30	86	this work

Table S3. The resistance of HER of the prepared samples (n = 3)

Sample	R_s/Ω	R_{ct}/Ω
P-$CoMoO_3$/MoO_2	2.8 ± 0.02	2.7 ± 0.03
$CoMoO_4$-Ar	3.3 ± 0.03	79.1 ± 0.02
$CoMoO_4$	3.3 ± 0.02	211.9 ± 0.02

Table S4. The radio of MoO_2 and $CoMoO_3$ in P-$CoMoO_3$/MoO_2 before and after the HER stability test (n = 3)

	MoO_2/%	$CoMoO_3$/%
Before stability test	26.0 ± 0.1	74.0 ± 0.2
After stability test	29.4 ± 0.2	70.6 ± 0.1

Table S5. The radio of MoO_2 and $CoMoO_3$ in P-$CoMoO_3$/MoO_2 obtained by calcination at different temperatures (n = 3)

	MoO_2/%	$CoMoO_3$/%	$CoMoO_4$/%
P-$CoMoO_3$/MoO_2-300	0.0 ± 0.1	0.0 ± 0.1	100.0 ± 0.1
P-$CoMoO_3$/MoO_2-400	12.0 ± 0.2	0.0 ± 0.1	88.0 ± 0.3
P-$CoMoO_3$/MoO_2-500	26.0 ± 0.1	74.0 ± 0.2	0.0 ± 0.1
P-$CoMoO_3$/MoO_2-600	42.3 ± 0.3	57.7 ± 0.2	0.0 ± 0.1

Table S6. The overpotentials and Tafel slopes of P-$CoMoO_3/MoO_2$ obtained by calcination at different temperatures (n = 3)

□	Overpotential/mV			Tafel slope /mV dec^{-1}
	100 mA cm^{-2}	500 mA cm^{-2}	1000 mA cm^{-2}	
P-$CoMoO_3/MoO_2$-300	-89 ± 2	-213 ± 1	-315 ± 3	161.3 ± 0.4
P-$CoMoO_3/MoO_2$-400	-93 ± 1	-200 ± 2	-278 ± 2	115.4 ± 0.2
P-$CoMoO_3/MoO_2$-500	-86 ± 2	-185 ± 1	-246 ± 1	58.7 ± 0.4
P-$CoMoO_3/MoO_2$-600	-115 ± 3	-239 ± 3	-319 ± 1	109.3 ± 0.3

Table S7. The radio of MoO_2 and $CoMoO_3$ in P-$CoMoO_3$/MoO_2 were obtained by calculating the different amounts of NaH_2PO_2 (n = 3)

	MoO_2/%	$CoMoO_3$/%	$CoMoO_4$/%
P-$CoMoO_3$/MoO_2-2	13.6 ± 0.2	36.4 ± 0.2	50.0 ± 0.3
P-$CoMoO_3$/MoO_2-4	14.3 ± 0.3	50.0 ± 0.1	35.7 ± 0.2
P-$CoMoO_3$/MoO_2-6	26.0 ± 0.1	74.0 ± 0.2	0.0 ± 0.1
P-$CoMoO_3$/MoO_2-8	20.8 ± 0.2	79.2 ± 0.1	0.0 ± 0.3

Table S8. The overpotentials and Tafel slopes of P-$CoMoO_3/MoO_2$ were obtained by calculating the different amounts of NaH_2PO_2 (n = 3)

□	Overpotential/mV			Tafel slope /mV dec^{-1}
	100 mA cm^{-2}	500 mA cm^{-2}	1000 mA cm^{-2}	
P-$CoMoO_3/MoO_2$-2	-125 ± 2	-249 ± 3	-328 ± 1	163.1 ± 0.3
P-$CoMoO_3/MoO_2$-4	-114 ± 3	-227 ± 1	-292 ± 2	128.9 ± 0.2
P-$CoMoO_3/MoO_2$-6	-86 ± 3	-185 ± 2	-246 ± 3	58.7 ± 0.2
P-$CoMoO_3/MoO_2$-8	-100 ± 3	-207 ± 2	-278 ± 1	94.8 ± 0.4

References

1. L. Wei, M. Du, R. Zhao, F. Lv, L. Li, L. Zhang, D. Zhou and J. Su, *Journal of Materials Chemistry A*, 2022, **10**, 23790-23798.
2. G. Kresse and J. Hafner, *Physical Review B*, 1994, **49**, 14251-14269.
3. J. F. G. Kresse *COMPUTATIONAL MATERIALS SCIENCE*, 1996, **6**, 15 - 50.
4. G. Kresse, *PHYSICAL REVIEW B*, 1996, **54**, 11169 - 11186.
5. D. J. Chadi, *Physical Review B*, 1977, **16**, 1746-1747.
6. F.-H. Yuan, M.-R. Mohammadi, L.-L. Ma, Z.-D. Cui, S.-L. Zhu, Z.-Y. Li, S.-L. Wu, H. Jiang and Y.-Q. Liang, *Rare Metals*, 2022, **41**, 2624-2632.
7. S. Sajjad, C. Wang, X. Wang, T. Ali, T. Qian and C. Yan, *Nanotechnology*, 2020, **31**.
8. M. Fang, W. Gao, G. Dong, Z. Xia, S. Yip, Y. Qin, Y. Qu and J. C. Ho, *Nano Energy*, 2016, **27**, 247-254.
9. Z. Zhang, X. Ma and J. Tang, *Journal of Materials Chemistry A*, 2018, **6**, 12361-12369.
10. X.-D. Wang, H.-Y. Chen, Y.-F. Xu, J.-F. Liao, B.-X. Chen, H.-S. Rao, D.-B. Kuang and C.-Y. Su, *Journal of Materials Chemistry A*, 2017, **5**, 7191-7199.
11. J. Tian, N. Cheng, Q. Liu, X. Sun, Y. He and A. M. Asiri, *Journal of Materials Chemistry A*, 2015, **3**, 20056-20059.
12. L. Chen, H. Wang, L. Tan, D. Qiao, X. Liu, Y. Wen, W. Hou and T. Zhan, *Journal of Colloid and Interface Science*, 2022, **618**, 141-148.
13. H. Cheng, Q. Liu, Y. Diao, L. Wei, J. Chen and F. Wang, *Advanced Functional Materials*, 2021, **31**.
14. Y. Lu, X. Zheng, Y. Liu, J. Zhu, D. Li and D. Jiang, *Inorganic Chemistry*, 2022, **61**, 8328-8338.
15. S. M. N. Jeghan, J. Kim and G. Lee, *Applied Surface Science*, 2021, **546**.
16. Y. Lin, D. Zhang and Y. Gong, *Applied Surface Science*, 2021, **541**.
17. Y. Gao, H. Ding, X. Fan, J. Xiao, L. Zhang and G. Xu, *Journal of Colloid and Interface Science*, 2023, **648**, 745-754.
18. X. Chen, Q. Li, Q. Che, Y. Chen and X. Xu, *ACS Sustainable Chemistry & Engineering*, 2018, **7**, 2437-2445.
19. B. Wang, X. Chen, Y. He, Q. Liu, X. Zhang, Z. Luo, J. V. Kennedy, J. Li, D. Qian, J. Liu and G. I. N. Waterhouse, *Applied Catalysis B: Environment and Energy*, 2024, **346**.
20. J. Sun, G. Ren, S. Qin, Z. Zhao, Z. Li, Z. Zhang, C. Li and X. Meng, *Nano Energy*, 2024, **121**.
21. E. Sadeghi, S. Chamani, E. Erdem, N. S. Peighambardoust and U. Aydemir, *ACS Applied Energy Materials*, 2023, **6**, 7658-7671.
22. L. Yu, Y. Xiao, C. Luan, J. Yang, H. Qiao, Y. Wang, X. Zhang, X. Dai, Y. Yang and H. Zhao, *ACS Applied Materials & Interfaces*, 2019, **11**, 6890-6899.
23. E. Hu, Y. Yao, Y. Chen, Y. Cui, Z. Wang and G. Qian, *ACS Applied Energy Materials*, 2021, **4**, 6740-6748.
24. Y. Ou, L. Liu, X. Peng, L. Zhang, Z. Ou, W. Zhang and Y. Zhang, *Nano Materials Science*, 2024, **6**, 565-575.
25. L. Zhao, L. Wei, H. He, X. Zhang, S. Liu and J. Wang, *International Journal of Hydrogen Energy*, 2024, **62**, 119-126.